

# Embedding Deep Learning in Inverse Scattering Problems

Yash Sanghvi, Yaswanth Kalepu, *Student Member, IEEE*, and Uday K Khankhoje, *Senior Member, IEEE*

**Abstract**—We introduce a Deep Learning based framework to solve electromagnetic inverse scattering problems. This framework builds on and extends the capabilities of existing physics-based inversion algorithms. These algorithms, such as the Contrast Source Inversion, Subspace-Optimization Method and their variants face a problem of getting trapped in false local minima when recovering objects with high permittivity. We propose a novel Convolutional Neural Network architecture, termed the Contrast Source Network, that learns the noise space components of the radiation operator. Together with the signal space components directly estimated from the data, we iteratively refine the solution and show convergence to the correct solution in cases where traditional techniques fail without any significant increase in computational time. We also propose a novel multi-resolution strategy that helps in producing high resolution solutions without any significant increase in computational costs. Through extensive numerical experiments, we demonstrate the ability to recover high permittivity objects which include homogeneous, heterogeneous, and lossy scatterers.

**Index Terms**—inverse scattering, contrast source inversion, subspace-based optimization, deep learning, convolutional neural networks

## I. INTRODUCTION

Electromagnetic inverse scattering problems (ISP) deal with reconstructing the spatial permittivities of unknown objects by measuring the scattered electromagnetic fields with a few receivers. It is well-known that the ISP is an ill-posed and non-linear problem (in terms of the object permittivity), leading to a large variety of numerical solutions being proposed such as the Born iterative method (BIM) [1–4] and the Distorted Born iterative method (DBIM) [5] which involve iterative solutions to the problem. Another class of iterative methods decouple the non-linear problem into data and state equation and optimize over an objective function involving the two terms. Contrast Source Inversion (CSI) [6–8] and Subspace based Optimization (SOM) [9–13] are examples of such numerical techniques. Yet another approach to combat the non-linearity of the inverse problem has been to use data collected at multiple frequencies [14], [15]. Recently, a family of new integral equations (NIE) [12] along with a new inversion method have been proposed to account for the global non-linearity of the problem and have shown to reconstruct scatterers with high permittivity and large electrical dimensions, something which the aforementioned techniques failed to achieve.

Deep learning (DL), and more specifically convolutional neural networks (CNNs), have enjoyed a great deal of recent

success in computer vision tasks such image recognition [16–18] and object detection [19], [20]. They have also been successfully employed to solve inverse problems as well; we refer the reader to [21] for an extensive review of how deep learning tools have been used to solve inverse problems of different kinds such as denoising, inpainting, nonblind image deconvolution, super-resolution etc. Earlier machine learning based techniques like support vector machines (SVMs) [22], [23] and neural networks [24–27] were employed to solve the ISP with varying levels of success. More recent formulations have employed CNNs for greater success. For example, [28] employed a three-layer CNN for super-resolution of inverse scattering solutions and [29] formulated deep-learning schemes for ISP which were able to generate quick, good quantitative results by training the U-Net [30], a unique CNN architecture originally designed for bio-medical segmentation.

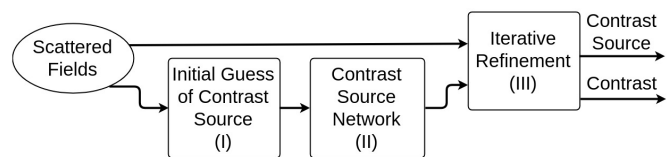


Fig. 1: Proposed pipeline for incorporating deep learning in inverse scattering solutions: An initial guess of the contrast source is generated using the scattered field in (I), this is used as input to a convolutional neural network, which generates an estimate of the total contrast source in (II), and finally this estimate is refined in (III) using iterative strategies such as variations of SOM and CSI to obtain a final solution.

On the one hand, it might be tempting to use DL to directly learn the relation between the scattered fields and the object permittivity. However, this idea has a few drawbacks. The neural networks trained to solve the inverse problem are relatively obscure models which are difficult to interpret and there is no direct way to incorporate prior knowledge about the unknown signal into the solution. These drawbacks have led researchers to look for ways to integrate deep learning into existing and well-understood techniques. For example, [31], [32] trained a neural network which could learn the underlying signal prior and could be used as a proximal operator in optimization-based approaches to solve inverse problems. Similarly, [33] mapped the well known alternating direction method of multipliers (ADMM) algorithm to a data-flow graph with trainable parameters such as the image transforms, shrinkage functions; this method achieved improved reconstruction accuracy in a compressed sensing-MRI system

Y. Sanghvi (e-mail:sangvhiyash95@gmail.com), Y. Kalepu (e-mail:yaswanthkalepu@gmail.com) and U. K. Khankhoje (e-mail:uday@ee.iitm.ac.in) are with the Dept. of Electrical Engineering, Indian Institute of Technology Madras, Chennai, India, 600036.

without any increase in computational time.

In this paper, we show how to effectively use Deep Learning in ISPs with a similar spirit of integration into existing techniques. It is well known that the relation between the scattered fields and object permittivity is nonlinear. However, the relation between the scattered fields and an intermediate variable (the contrast source) is linear. In order to avoid challenging nonlinear inversion techniques, we work with the contrast source variable, where we are faced with a linear inverse problem, and our solution strategy is inspired by the *DeepInverse* network [34]. The proposed method can be divided into three stages as shown in Figure 1:

- (Stage I) An initial guess of the contrast source,
- (Stage II) a forward pass through a custom CNN to obtain a better estimate of the contrast source,
- (Stage III) further refinement using an iterative optimization procedure.

In the absence of Deep Learning, Stage I would directly feed to Stage III. Through numerical experiments, we demonstrate that the proposed method is able to reconstruct objects of much higher permittivity than the original versions of these methods (minus Deep Learning), could have reconstructed.

The paper is organized as follows. Section II explains the problem statement and defines the problem notation. Section III motivates the Deep Learning framework and describes the three stages mentioned above. Section IV describes the implementation details, involving how to estimate the signal-space components of the contrast source, the training of the CNN, and a finally a multi-resolution strategy to estimate high resolution objects by using results of low resolution inversions. Numerical experiments are discussed in Section V, where various types of objects are reconstructed by existing and the proposed technique. Finally, the paper is concluded in Section VI with a short summary and directions for future extension.

## II. PROBLEM DEFINITION

In this paper we investigate a two dimensional (2D) transverse magnetic (TM, i.e.  $E_z$  polarization) inverse scattering problem (ISP). The object of interest is within an imaging domain  $D$  and has complex permittivity varying in the  $x - y$  plane. The relationship between the total, incident and scattered field ( $E, E^{(i)}, E^{(s)}$ , respectively), and complex permittivity,  $\epsilon(\vec{r})$ , is given by an integral equation of Fredholm type [35]:

$$E(\vec{r}) - E^{(i)}(\vec{r}) = E^{(s)}(\vec{r}) = \iint_D G(\vec{r}, \vec{r}') \chi(\vec{r}') E(\vec{r}') d\vec{r}' \quad (1)$$

where  $\chi(\vec{r}) = \epsilon(\vec{r}) - 1$  denotes the contrast of the object. The scattered field is measured with  $N_S$  receivers per illumination with a total of  $N_I$  illuminations in a single experiment. For sake of numerical experiments, we solve the discretized version of the Eq. (1) by partitioning  $D$  into an  $M \times M$  square grid using the method of moments [35]. Defining a ‘contrast source’ variable (sometimes referred to as the induced current) as the product of the contrast ( $x$ ) and the internal field ( $d$ ) at any point in  $D$ , we get the following associated discretized

equations (the first two are referred to as ‘state’ and ‘data’ equations, respectively):

$$d_n = e_n + G_D w_n \quad (2a)$$

$$s_n = G_S w_n \quad (2b)$$

$$w_n = X d_n = X e_n + X G_D w_n \quad (2c)$$

where  $d_n \in \mathbf{C}^{M^2 \times 1}$ ,  $e_n \in \mathbf{C}^{M^2 \times 1}$  refer to the total internal and incident fields for the  $n^{th}$  illumination, respectively,  $w_n \in \mathbf{C}^{M^2 \times 1}$  refers to the contrast source,  $s_n \in \mathbf{C}^{N_S \times 1}$  refers to the scattered field,  $x \in \mathbf{C}^{M^2 \times 1}$  refers to the contrast of the imaging domain, while  $X \in \mathbf{C}^{M^2 \times M^2}$  is the diagonal form of the vector  $x$ . Finally,  $G_S \in \mathbf{C}^{N_S \times M^2}$  and  $G_D \in \mathbf{C}^{M^2 \times M^2}$  are discrete versions of the radiation operators.

The inverse scattering problem is to estimate  $x$  given noisy measurements,  $s_n + \eta$ , where  $\eta$  denotes noise, for various illuminations ( $n$ ), and as is typically assumed,  $e_n$  is taken to be known.

## III. METHODS

### A. Motivation

The ill-posedness of the inverse scattering problem (ISP) stems from the fact that the measurements  $s_n$  in Eq. (2b) come from an under-determined system of equations. Further, it can be seen from Eq. (2) that to solve the inverse problem, a non-linear and ill-conditioned system of equations between the scattered fields and the object contrast have to be inverted. Such a system will have infinite solutions, and hence some form of regularization that incorporates prior information, is required to pick out a meaningful solution. However the choice of regularization term is not straightforward in this case, as there is no well-known prior which could be employed for a general contrast source image.

To obtain a better estimate of the contrast source from the linear set of equations from Eq. (2b) using the underlying prior, we look towards deep-learning (DL) based approaches. Specifically, we adopt the approach in [34] where a CNN is trained to learn both a representation of the signals and an inverse map approximating a greedy/convex recovery algorithm. This technique, known as *DeepInverse*, performs at-par with state-of-the-art compressive sensing solvers but takes significantly less run time. In a similar spirit, we propose a three stage DL solution to the ISP which learns and exploits the underlying prior of contrast source images and is able to reconstruct strong scatterers. The overall framework has been elucidated in Fig. 1, and we now expand on the individual stages.

### B. Initial Guess (Stage - I)

Similar to the approach taken in SOM, we partition the contrast source into signal and noise subspace components based on the singular values of the  $G_S$  operator, i.e.  $w = w^s + w^n$ . The former are uniquely determined by the  $L$ -term truncated singular value decomposition (SVD) as follows:

$$w^s = \sum_{i=1}^L \frac{u_i^H s}{\sigma_i} v_i \quad (3)$$

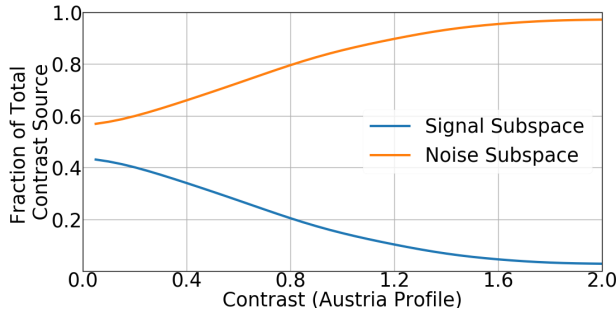


Fig. 2: Relative distribution of true contrast-source variable intensity between signal and noise subspaces, studied as a function of increasing values of dielectric contrast of Austria profile object discussed subsequently in the text (see Fig. 7(a)).

where  $u, v$  represent the left and right singular vectors, and  $\sigma$  the corresponding singular values in the SVD of  $G_S$ . The signal subspace is spanned by the first  $L$  ( $\leq N_S$ ) right singular vectors and noise subspace is spanned by the remaining. The choice of  $L$  is crucial and its selection is defined in Section IV. Defining a basis for the latter subspace as  $V_N = [v_{L+1} \dots v_{M^2-L}]$ , the complete contrast source can be expressed as

$$w = w^s + V_N \alpha \quad (4)$$

where  $\alpha$  are coefficients of the basis vectors for the noise subspace and are as yet unknown.

Therefore, as an initial guess of the contrast source we use the signal subspace component  $w^s$ ; this is used as input to the CNN in the subsequent stage.

### C. Contrast Source Network (Stage - II)

We propose a novel CNN architecture, termed as the Contrast Source Net (*CS-Net*), which takes as input the signal subspace of the contrast source and outputs an estimate of the total contrast source. It does so by learning the underlying prior of similar contrast source images which are generated from homogeneous scatterers of varying permittivities.

It is found by extensive numerical studies that the fraction of energy of the contrast source in the noise subspace increases steadily as the contrast of the object is increased, seen graphically in Fig. 2 for a popular benchmark object known as the ‘Austria’ profile (more details in Section IV). Thus, the part of the solution that can be estimated from the scattered field data alone, the signal subspace component, becomes lesser as the contrast increases, highlighting the challenge of ISPs.

It is worth noting that the above challenge manifests in a different form when the ISP is formulated directly with the contrast as the variable of optimization. Here we find that there are several local minima seen in the proximity of the path from the origin to the true solution [36], and the solution get stuck in any one of them.

Traditional iterative strategies such as the SOM or CSI typically initialize the search for the noise space components (i.e. the  $\alpha$ ’s in Eq. (4)) from the origin, thereby increasing the

chances of falling into corresponding local minima on the way to the global minima. At the heart of our innovative strategy is this: we *learn* the noise subspace components using our custom CS-Net. As a result, the local minima issue is avoided for a larger range of object permittivities than previously possible.

### D. Iterative Refinement (Stage - III)

The third stage aims at refining the contrast source estimate obtained at the output of *CS-Net*. This is done by optimizing a objective function involving state and data equation terms and initializing the variables in optimization using the contrast source estimate obtained from previous stage. In principle, one can employ cost functions similar to those used in CSI or variants of SOM initialized by estimates of contrast source obtained from the previous stage. In this paper, we limit the discussion to SOM and one of its variations, two-fold SOM (TSOM) [10]. Additionally, we also impose an additive total variation (TV) regularizer on contrast images, terming the resulting inversion strategies as either ‘SOM+TV’ or ‘TSOM+TV’. This regularization is applicable for piece-wise constant scatterers and a similar strategy has been recently used [37].

As mentioned above, there are many choices of objective functions which one can choose to optimize as a part of Stage - III. For example, an objective function which employs TSOM+TV is as follows:

$$F(\beta_1, \beta_2, \dots, \beta_{N_I}, X) = \sum_{n=1}^{N_I} \left( \frac{\|s_n - G_S(w_n^s + V_D' \beta_n)\|_2^2}{\|s_n\|_2^2} + \frac{\|A\beta_n - b_n\|_2^2}{\|w_n^s\|_2^2} \right) + \gamma \|TV(x)\|_1 \quad (5)$$

$$\text{where } A := (I - XG_D)V_D', \quad (6)$$

$$b_n := Xe_n - (I - XG_D)w_n^s, \quad (7)$$

$$V_D' := (I - V_S^{(L)}V_S^{(L)H})V_D^{(M_0)} \quad (8)$$

$$TV(x) = \begin{bmatrix} D^v & 0 \\ D^h & 0 \\ 0 & D^v \\ 0 & D^h \end{bmatrix} \begin{bmatrix} \Re(x) \\ \Im(x) \end{bmatrix} \quad (9)$$

such that  $V_S^{(L)}, V_D^{(M_0)}$  are matrices with top  $L, M_0$  right singular vectors of  $G_S, G_D$  matrices respectively,  $D^h, D^v$  are matrices representing the first order horizontal and vertical difference operators respectively,  $\Re(x), \Im(x)$  denote the real and imaginary components of  $x$ , respectively,  $V_D' \beta_n$  represents the null space components of the contrast source, and  $H$  represents conjugate transpose of a matrix.  $M_0$  is a hyper-parameter used in TSOM which affects the regularization on the contrast source domain by controlling the subspace to which it can belong.

As noted earlier, in the original versions of the above iterative techniques, the noise subspace coefficients are initialized to zero whereas in the proposed method they are estimated in Stage - II.

### E. Comparison with related schemes

A popular method of dealing with the non-linearity of the inverse problem has been to use multi-frequency data [14], [15]. These are based on the principle that lower frequency reconstructions are less affected by the issue of non-linearity, hence these reconstructions can be used as a priori information for high frequency reconstructions which would otherwise fail. The difference between these and our methods can be conceived of as the manner in which a priori information is incorporated; in one case from lower frequency data, and in our case, from the *CS-Net* at a single frequency. We compare these two approaches via numerical results in Section V-B.

A related DL-based inversion procedure, the Dominant Current Scheme (DCS) was recently proposed [29] to solve the ISP. The DCS estimates the induced current ( $w$ ) and obtains the contrast ( $x$ ) from it; this contrast is used as input to a trained U-Net and the output is used as the final solution for each illumination. The DCS and our scheme use different inputs to the corresponding CNNs, as the former trains the U-Net on contrast and the latter trains the *CS-Net* on the contrast source. Another significant difference between the two schemes is that the DCS is aimed at obtaining a good quantitative result as quickly as possible, while our scheme is aimed at retrieving high contrast objects by leveraging existing schemes.

## IV. IMPLEMENTATION DETAILS

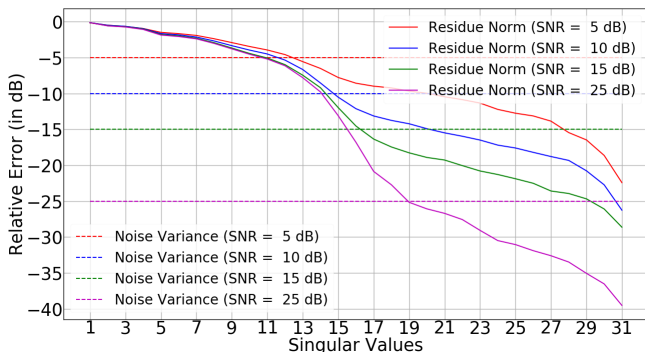


Fig. 3: This plot displays the variation of the scattered field residue norm, estimated as  $\|s - G_{sw}^s\|^2$ , with number of singular values  $L$  used in Stage - I and compares it with the noise variance for different values of SNR. The scattered field used to plot the figure is obtained from the Austria profile of contrast 2.

### A. Morozov's Discrepancy Principle

In order to implement Stage - I of our algorithm, we need to determine the number of singular values,  $L$ , to be used to define the signal subspace as per Eq. (3). The optimal choice for number of singular values varies with the signal to noise ratio (SNR) of the measurements and is determined from Morozov's discrepancy principle [38]. It states that the optimal values  $L$  is chosen as the least value for which the norm of the residue from the data equation comes within a

(close to unity) factor of the noise variance – in other words,  $L$  is chosen such as to avoid fitting the noise. The variation of the residue norm with  $L$  is shown in Fig. 3. In our numerical experiments, we add synthetic noise with  $SNR = 25dB$  to the scattered fields, and so  $L = 19$  is the optimal choice for number of singular values as evident from Fig. 3.

Our general assumption is that in a given experimental setup, the SNR values will be known, or can be estimated using calibration targets. For whatever reason, if this is not possible, it is important to assess the performance of the proposed scheme for a variety of SNR values. As can be seen from Fig. 3, the optimum value of  $L$  varies from 13 to 19 as SNR goes from 5 to 25 dB. In the absence of exact knowledge of SNR, as suggested in [9], the value of  $L$  can be chosen empirically to be the point where the singular values “noticeably change the slope in the spectrum” of singular values of the scattering operator. In our numerical studies, we have found that the performance is not very sensitive to the chosen  $L$  number, an observation that has also been made previously [9].

### B. CS-Net: Architecture and Training

The architecture details of the Contrast Source Network (CS-Net) used for estimation of noise subspace components are described in detail in Fig.4. The first layer of the network consists of convolutional filters of varying sizes. The convolution across the channels of the image ensure that information from multiple illuminations is combined and different filter sizes are used to capture features from different spatial scales. A similar convolutional layer is used in the last layer to convert the penultimate stage into a contrast source image.

The training procedure for the CNN is as follows:

- (1) The MNIST dataset [39] consisting of 60,000 digit images of size  $28 \times 28$  pixels, are used to generate the contrast images (See Fig. (6) for samples). The digits image are re-scaled to  $16 \times 16$  pixels and multiplied by a random number such that the resulting image has maximum contrast lying uniformly between 1 and 7.
- (2) These images are now treated as dielectric objects, and are given as input to a method of moments based forward solver [35] to generate internal electromagnetic fields; hence a corresponding contrast source image is generated for each illumination (since contrast source is defined as the product of the contrast with the internal field at each pixel within the object per Eq. (2c)).
- (3) The network is trained with the average mean squared loss between estimated and true induced current and the network parameters are tuned with Adam optimizer [40] with learning rate  $10^{-4}$ .

We note that the ‘strength’ of a scatterer is roughly given in terms of the product of the contrast and an approximate size of the scatterer [41], and it is important for there to be parity between the strength of the scatterers in the training and testing stages. Since the digit-like objects from the MNIST database have many features that are ‘thin’ (see Fig. (6)), it is necessary to train the CS-Net on digit-like objects with much higher contrast if the CS-Net is going to be applied to different, larger objects during the testing phase.

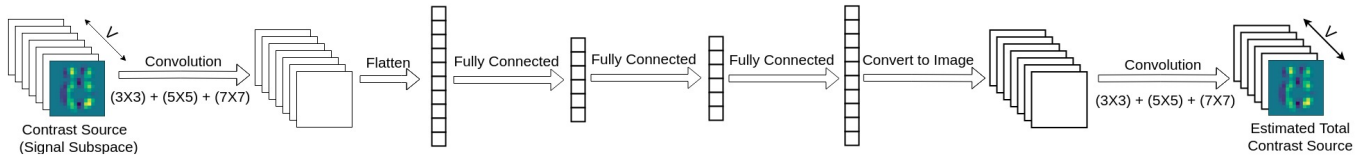


Fig. 4: Architecture details of *CS-Net*. The network takes into input the signal subspace of the contrast source and outputs an estimate of the true contrast source. The input is represented as  $16 \times 16$  image with  $V = 16$  channels. The first layer performs convolution with different filter sizes i.e.  $(3 \times 3)$ ,  $(5 \times 5)$ ,  $(7 \times 7)$ , and  $(9 \times 9)$ , each with 8 channels, and stacks the filter activations to form a  $16 \times 16$  image with 32 channels. The image is then vectorized and passed through 3 fully connected layers, each with a ReLU activation. The output vector is reshaped to an 8 channel  $16 \times 16$  image again and a last convolution layer is used to generate the estimate of true contrast source.

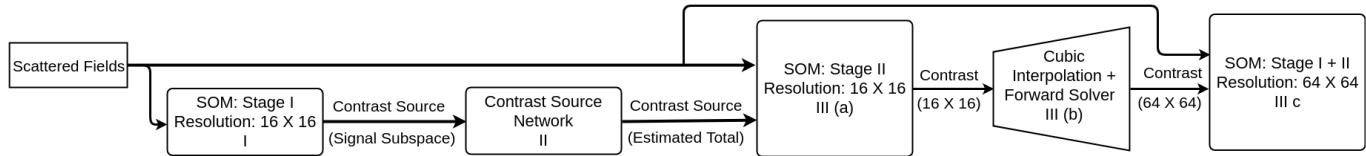


Fig. 5: Proposed scheme for integrating deep learning in SOM. Firstly, the signal subspace of contrast source is obtained at a low resolution Stage - I and pushed through the contrast source network to obtain an estimate of the total contrast source (Stage - II). The noise subspace components of the estimate from Stage - II are used to initialize noise subspace of contrast source in Stage-III and hence used to obtain a low resolution estimate of the contrast. This initial guess is interpolated using cubic interpolation to a high resolution and used to initialize Stage - III(c) at that resolution. See text in Sec. (IV-D) for further details.

### C. Optimization Procedure in Stage - III

In Stage - III, an objective function in terms of noise subspace and contrast variables, e.g. Eq. (5), are optimized by an alternative optimization strategy commonly used in SOM or CSI type algorithms. First, the contrast source noise subspace components (i.e.  $\beta$ 's) are updated using Polak-Ribiere conjugate gradient method. Then, the contrast variables ( $X$ ) in Eq. (5) are updated using 20 sub-iterations of the ADMM algorithm [42]; the latter algorithm provides a convenient way of solving TV regularization problems by variable splitting [43].

Note that in absence of the additive TV regularization term, the contrast update can be formulated as a least squares problem which has a closed form solution, as suggested in the original version of SOM [9]. The optimization procedure is terminated when either the relative change in cost function falls below  $10^{-4}$  or 2000 iterations are complete, whichever happens first.

### D. Multi-Resolution Strategy

In designing the *CS-Net*, we are faced with a design choice between image resolution and the training time. While the resolution of MNIST dataset images is sufficient to represent high contrast ( $x$ ) objects, it is not possible to represent the corresponding internal fields ( $d$ ), and therefore the contrast source variables ( $w$ ) at the *same* resolution. This is because of the fact that as the contrast value increases, the spatial frequencies of the internal fields increase, and need finer resolution for representation in the pixel domain. On the other hand, the computational burden during the learning phase will increase significantly if we train on high resolution images.

To resolve this issue, we instead propose a multi-resolution strategy where we take a middle ground by training on lower resolution images and then up-scale the learned image before the final iterative stage, effectively applying the SOM twice with variations. As an example, the entire multi-resolution strategy, using TSOM+TV for contrast source refinement, is explained in detail in Fig. 5. The key steps are as follows:

- (1) In Stage - II, the *CS-Net* takes as input contrast source images of size  $16 \times 16$  pixels and outputs contrast source estimate of the same size
- (2) The preceding output is sent to Stage - III (employing a SOM algorithm) which produces a contrast estimate of size  $16 \times 16$  pixels.
- (3) This contrast is up-scaled to size  $64 \times 64$  pixels using cubic interpolation.
- (4) The forward solver is run on this up-scaled contrast image to generate the contrast source images,  $w'$ , at this higher resolution. The noise space estimates are obtained by projecting  $w'$  onto the noise subspace.
- (5) The signal space components are obtained by running Stage - I on the scattered field at the higher resolution. Together with the noise space estimates from the earlier step, a final iterative strategy (like SOM/TSOM+TV) is used to recover the contrast at the desired, higher resolution.

## V. NUMERICAL EXPERIMENTS

In this section, we describe the numerical experiments through which we compare the proposed scheme and its non-Deep Learning (DL) counterparts. Throughout, we assume the object is confined in a square domain of side  $2m$ ; the incident field frequency is 400 MHz (i.e. wavelength  $\lambda = 0.75m$ );

measurements are taken on a circle of radius  $R_s = 4m$ , with the center of the circle coinciding with the center of the object domain;  $N_s = 32$  receivers are placed on the measurement domain in an equiangular manner, and  $N_i = 16$  transceivers are placed on a circular domain of radius  $R_i = 6m$  for different illuminations. We generate the scattered field using a forward solver [35] at a resolution of  $100 \times 100$  pixels. Unless otherwise mentioned, the scattered field is corrupted with additive Gaussian noise such that the SNR is 25dB. To compare different schemes, we define the total and internal error (i.e. the mean relative error) between the ground truth and reconstructed profile as follows:

$$\text{Total Error} = \frac{1}{M^2} \sum_{i: [1, M^2]} \frac{|\epsilon_{t,i} - \epsilon_{r,i}|}{|\epsilon_{t,i}|}$$

$$\text{Internal Error} = \frac{1}{|S|} \sum_{i: S} \frac{|\epsilon_{t,i} - \epsilon_{r,i}|}{|\epsilon_{t,i}|}$$

where  $\epsilon_r$ ,  $\epsilon_t$  are the reconstructed and true (complex) permittivity profiles respectively and  $S$  is the support of the object.

All numerical experiments in this paper are performed on an Intel-i7 processor running at 3.45 GHz with 32GB RAM. The training procedure, which includes running the forward solver at each iteration, ran for 50 epochs, with each epoch consisting of 3000 iterations, totalling to approximately 36 hours.

### A. Homogeneous Scatterers

The first objects investigated are digit images from the test dataset in MNIST. The contrast source obtained as the output of the *CS-Net* is converted to the equivalent contrast image. No iterative strategy is used to obtain the solution in this case and the reconstruction results are shown in Fig. 6, showing a good quantitative match between the ground truth and the reconstructions.

Next, the proposed scheme is evaluated on the *Austria* profile for different contrasts; this consists of one central ring with inner and outer radius equal to  $0.3m$  and  $0.6m$  respectively and two disks each of radius equal to  $0.3m$ . The central ring's center is located at  $(0, 0.2m)$  and smaller disks are located at  $(-0.3m, -0.6m)$ ,  $(0.3m, -0.6m)$ . The profile is homogeneous and contrast of the rings and disks varies from 1 to 4, and the reconstruction results are displayed in Fig. 7. This figure also highlights the role that regularization plays in reconstructing high contrast objects; in particular the presence of a TV regularizer leads to a good solution as seen in Fig. 7(e), as compared to Fig. 7(f), where no such regularizer is applied. Additionally, we show the results of reconstructions when the SNR value of the scattered field data is different that what was used during training; in particular, Fig. 7(g),(h) show reconstructions for 10 and 15 dB, respectively. Evidently, as SNR values begin to degrade, so does the performance.

### B. Comparison with non Deep Learning approaches

In order to better appreciate the virtues of DL in solving the ISP, we compare the proposed scheme with a multiresolution strategy which does *not* contain a *CS-Net* in the pipeline, i.e. we run through the pipeline shown in Fig. (5) with

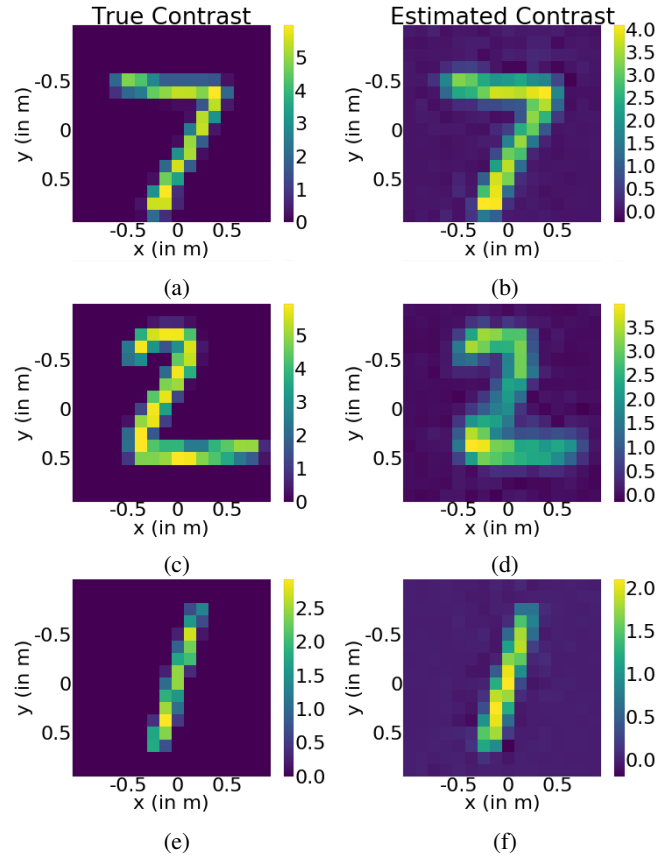


Fig. 6: Estimated contrast from *CS-Net* output on MNIST test images. The contrast source obtained as output from the network is used to calculate the contrast directly without any iterative strategy. The internal errors for reconstructions are **0.297**, **0.441** and **0.179** respectively. The colour bar in this and all subsequent images in the paper refer to the (real or  $-1 \times$ imaginary) value of the contrast.

Stage - II removed and the noise space components of the contrast source set to zero. Through this experiment, we aim to demonstrate the significance of deep learning in the pipeline.

Reconstructions of the *Austria* profile for a particularly challenging value of contrast equal to 4, using DL and non-DL version of the proposed schemes, are shown in Figure 8 and the respective errors of reconstructions are listed in Table I. As clearly observed from Figure 8e, the non-DL version of the scheme is trapped in a false minima due to unsuitable initialization of the noise subspace components. At contrast as high as 4 for the *Austria* profile, the noise subspace coefficients become more significant and as a result they cannot be initialized to zeros any more. Through the proposed DL-based framework, a rough estimate of the noise subspace for the strong scatterers is provided and hence the DL multi-resolution strategy converges closer to the true solution. We note however, that the *Austria* profile with contrast 5 fails to be reconstructed (with internal error 0.401), ostensibly due to a lack of such strong scatterers in the training database. The suggested solution for inverting objects of higher contrast is to

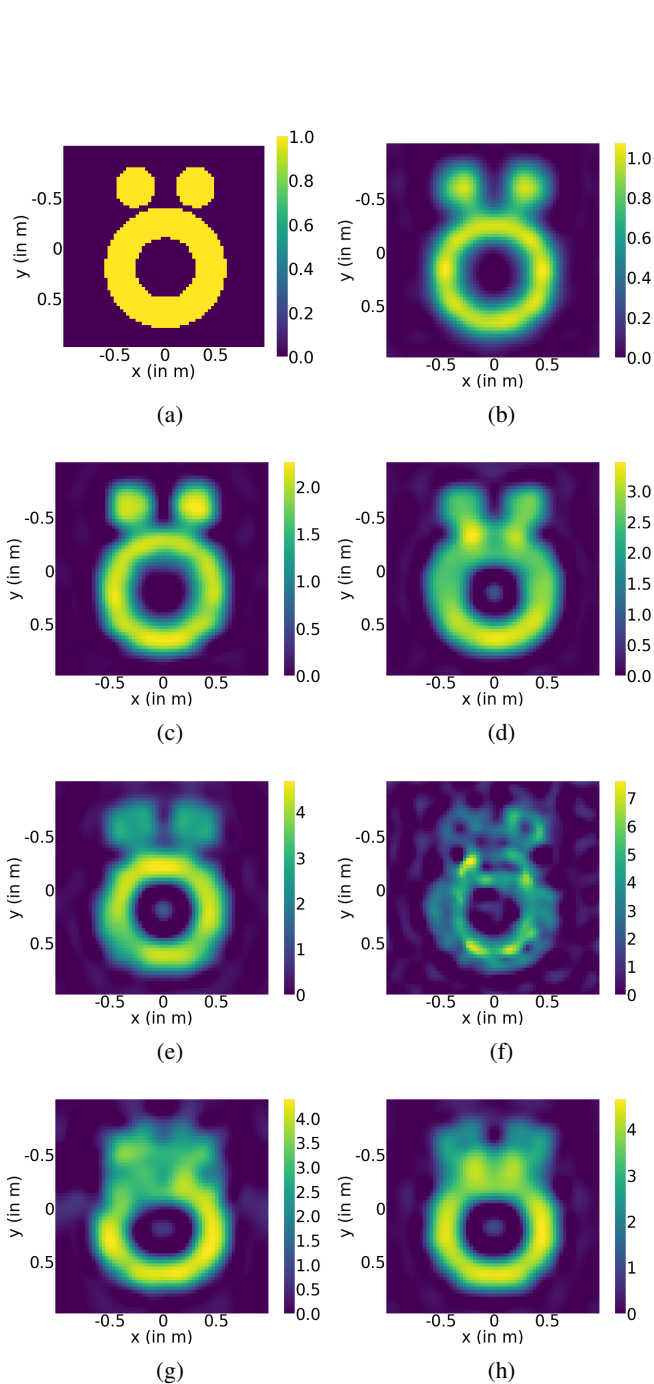


Fig. 7: (a) True *Austria* profile (b)-(e) Reconstruction of *Austria* profile for different contrasts using the proposed scheme (TSOM+TV with DL). The contrast of the true profiles are as follows: (b) **1.0** (c) **2.0** (d) **3.0** and (e) **4.0**. (f) *Austria* (contrast = 4) reconstruction with SOM with DL, in Stage-III at  $64 \times 64$  resolution (g), (h) *Austria* (contrast = 4) reconstructions with SNR = **10 dB** and **15dB** respectively. The respective internal errors are (b) **0.099** (c) **0.106** (d) **0.150** (e) **0.162** (f) **0.270** (g) **0.201** (h) **0.161**

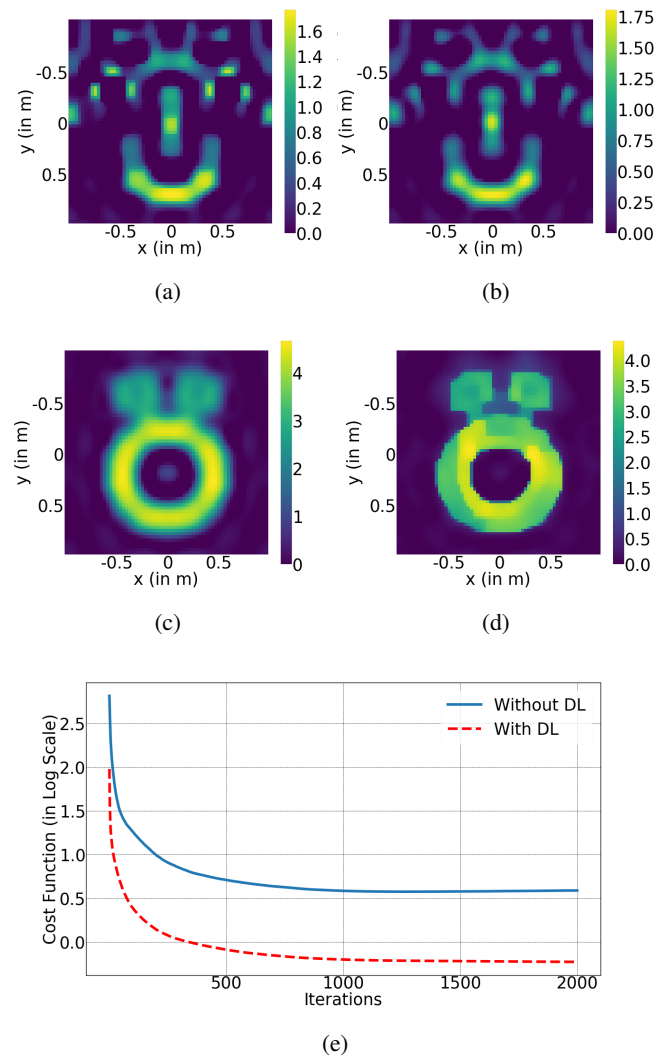


Fig. 8: Reconstruction results of *Austria* profile (contrast = 4) from (a) non-DL, TSOM+TV, (b) non-DL, SOM+TV, (c) DL, TSOM+TV (d) DL, SOM+TV, and (e) variation of cost function with iterations for the DL and non-DL variants of TSOM+TV. It is clear from the figure that non-DL multi-resolution scheme converges to a false minima. The respective internal errors of the reconstructions are (a) **0.711** (b) **0.712** (c) **0.162** (d) **0.150** respectively.

train the CS-Net with objects of higher electrical size (contrast and dimensions) and a larger image size (i.e. more pixels). The latter allows CS-Net access to more high frequency information of the contrast source due to the increased spatial resolution.

To demonstrate the generality of our scheme, we incorporate DL into both SOM+TV and TSOM+TV (recall that the latter regularizes the contrast source by considering a finite number of the singular vectors of the  $G_D$  operators in Eq. (2c)).

Inverse Scattering Technique	Internal Error	Total Error
SOM+TV without DL	0.711	0.328
TSOM+TV without DL	0.712	0.317
SOM with DL	0.270	0.438
SOM+TV with DL	0.150	0.223
TSOM+TV with DL	0.162	0.288

TABLE I: Reconstruction errors for Austria profile (contrast = 4.0) with different schemes. Whenever TSOM is used in Stage - III, the number of singular values of  $G_D$  operator, i.e.  $M_0$ , is set as 500.

Time (s) $\rightarrow$ Experiment $\downarrow$	Stage I	Stage II	Stage III(a)	Stage III(b)	Stage III(c)	Total Time
$x = 1, DL$	0.004	0.091	25.3	7.61	166	199
$x = 1, no DL$	0.004	-	31.8	7.62	155	194
$x = 4, DL$	0.002	0.011	95.5	55.9	4546	4697
$x = 4, no DL$	0.002	-	29.1	16.4	2746	2791*

TABLE II: Computational time taken for each stage of the methods for homogeneous Austria profile with different contrasts,  $x$ . ‘\*’ denotes experiments in which Stage III (c) converged to a false solution.

To further illustrate the above comparisons we show in Table II the stage-wise breakups of the compute times on reconstruction attempts of the benchmark Austria profile for both, deep learning (DL) and non-DL algorithms. As can be seen, higher contrasts lead to higher iteration times due to the increased nonlinearity of the problem. The time taken in the DL step is insignificant, and non-DL approaches fail for higher contrasts.

Based on Table II, it is clear that the iterative procedure in SOM Stage III(c) is the most time consuming part of the entire scheme and the forward pass through CS-Net takes a tiny fraction of the entire computational scheme. The iterative refinement portion of the Stage-III has computational complexity  $O(I \times N_I \times M^2 \log M)$  where  $I$  is the total number of iterations,  $N_I$  is the number of illuminations and  $M^2$  is the number of pixels in imaging domain. Each gradient and step calculation for a single view takes  $O(M^2 \log M)$  instead of  $O(M^4)$  as all matrix-vector operations with matrix  $G_D$  are performed using fast Fourier transform (FFT) operations.

To conclude this discussion on comparisons with non-DL schemes, we compare the proposed method with a conventional method used to address the issue of non-linearity: the multi-frequency (MF) approach [15], which has been discussed earlier. We consider two frequencies, 400MHz and a lower frequency (in our case: 100MHz and 200MHz). Using the MF approach we attempt to reconstruct an Austria profile object of contrast 4, using the reconstruction of the lower frequency to aid the reconstruction at 400 MHz. This numerical experiment for 200MHz ends in failure, as can be seen in Fig. 9(b). We repeat this experiment a second time, but with the use of the 100MHz solution as the initial guess for TSOM+TV at 400MHz. It is found that the object is successfully reconstructed, as seen in Fig. 9(a) and achieves a similar result as that of the DL-based method. Thus, to achieve similar results as that of the proposed scheme using multi-

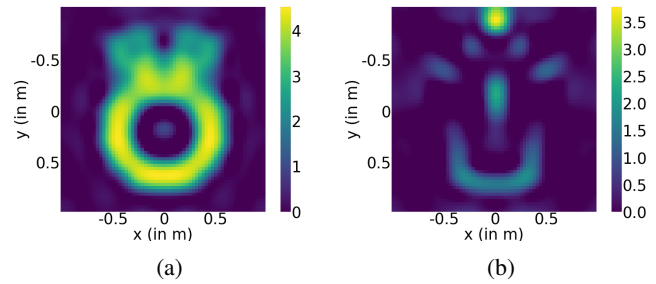


Fig. 9: Reconstruction of *Austria* profile for contrast = 4 using solution obtained from at lower frequencies to initialize TSOM+TV at 400MHz. The initial guess is provided by solution from (a) 100MHz and (b) 200MHz. The respective internal error numbers are (a) **0.159** (b) **0.714**

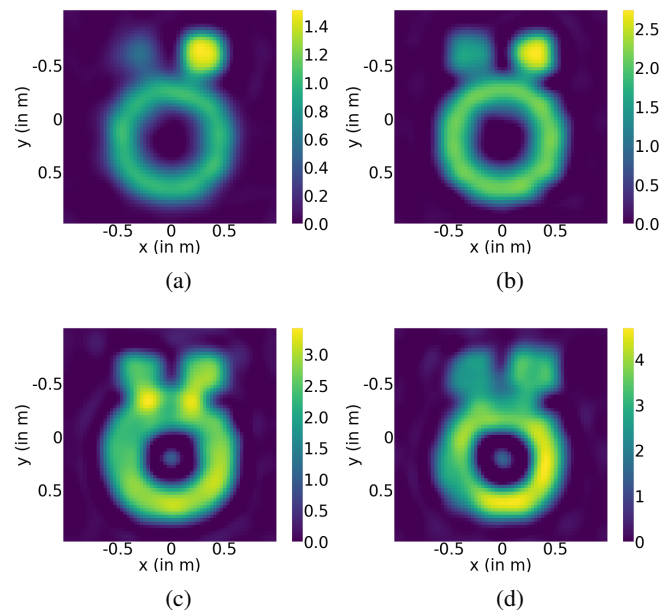


Fig. 10: Reconstruction of *Heterogeneous Austria* profile for different contrasts using the proposed scheme. The contrast of central ring in the true profiles are as follows (a) **1.0** (b) **2.0** (c) **3.0** and (d) **4.0**. The left circle has contrast 0.5 less than the central ring and the right circle has contrast 0.5 more than the central ring in the true profiles. The respective internal errors are (a) **0.094** (b) **0.107** (c) **0.153** (d) **0.205**.

frequency methods, scattered fields from frequency as low as 100MHz are required and thus lead to larger data acquisition times compared to the proposed scheme, which only requires single frequency data.

### C. Heterogeneous Scatterers

The contrast source network is trained using the contrast profile of homogeneous scatterers and hence one might argue that the proposed scheme might not give accurate results for objects where the contrast attains different values *within* the same object. We investigate this hypothesis numerically, and in Fig. 10 report the results of testing the proposed scheme

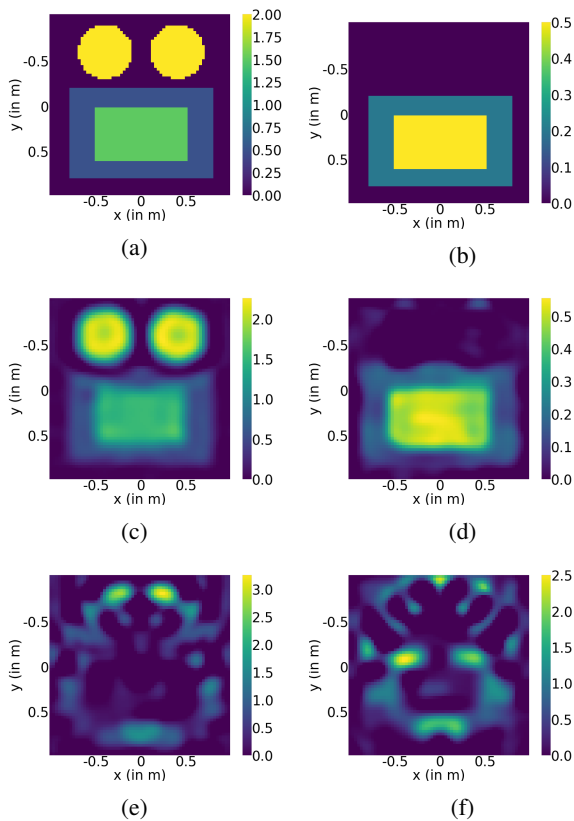


Fig. 11: (a) Real and (b) Imaginary part of the true lossy scatterers. Real and Imaginary part of reconstruction results using (c),(d) DL, TSOM+TV and (e),(f) non-DL, TSOM+TV. The respective internal errors are **0.091** and **0.512** respectively.

on the *Heterogeneous Austria* profile. This is spatially similar to the *Austria* profile; however the permittivity of the left disk is 0.5 less than that of the central ring and permittivity of the right disk is 0.5 more than that of the central ring. The reconstruction error is found to be similar to that in case of the homogeneous *Austria* profile.

As the results indicate, the proposed scheme can also reconstruct heterogeneous scatterers, since Stage - III ensures that the final contrast and noise subspace of contrast source are in agreement with the scattered field data by satisfying the data and state equations. The primary reason for this success is that even though the training is on homogeneous objects, those objects themselves contain multiple scattering interfaces (e.g. the two extremities of the digit “seven” scatter waves multiple times between each other); thus the network is implicitly trained to recognize multiple scattering that happen when the contrast is spatially heterogeneous.

#### D. Lossy Scatterers

After having demonstrated the proposed scheme on lossless objects, we now consider lossy scatterers (based on [11] but with higher values of the real part of the contrast). The scatterer consists of: disks of contrast 2.0 of radius  $0.3m$  located at  $(-0.4m, -0.6m)$  and  $(0.4m, -0.6m)$ ; two rectangles (of dimensions  $1m, 0.6m$  and  $1.6m, 1m$  respectively) each

centered at  $(0m, 0.3m)$  and have contrasts equal to  $1.5 - i0.5$  and  $0.5 - i0.2$ , as seen in Fig. 10. The reconstruction obtained through non-DL and DL versions of the proposed scheme are shown in Fig. 11.

It is clear from Fig. 11 that without DL the results are far from satisfactory. Even though the *CS-Net* has not explicitly been trained on lossy objects, its incorporation in TSOM+TV results in internal errors of less than 15% on such objects, thus conferring a large degree of generality on the *CS-Net*.

#### E. Reconstructions on Experimental Data

Having demonstrated numerical results on synthetic data, we now consider reconstructions obtained by running our algorithm on experimental scattered field data; in particular we use the so-called ‘Fresnel’ database [44], [45], and attempt the reconstruction of two inhomogeneous objects, *FoamDieIntTM* and *FoamTwinDieIntTM* using scattered field data obtained at 6 GHz (see Fig. 12(a),(b)). This high frequency has been chosen because it is particularly challenging for conventional, single-frequency methods to reconstruct (see Fig. 12(c),(d) for corresponding results. Correspondingly, the results of our method are shown in Fig. 12(e),(f) which demonstrate the success in reconstructing the objects with very low error (around 0.17). At lower frequencies, both methods give comparable results, thereby demonstrating the power of the proposed method at higher frequencies where the effect of nonlinearity is more.

#### F. Sensitivity of Training Configuration

An important consideration that comes up is the sensitivity of the proposed method to changes in the measurement configuration compared to what the *CS-Net* has been trained for. We discuss the sensitivity to the following setup parameters:

(1) Frequency: If the frequency is altered but all other experimental features are unchanged, e.g. the position of transmitters/receivers and object dimensions, then a drop in performance is observed, since the test configuration differs from the training. However, we find that the drop in performance is not abrupt. For e.g. the *CS-Net* was trained for experiments at 400 MHz, and was able to reconstruct the *Austria* profile of contrast 4. When we lowered the frequency to 300 MHz, we found that the same object with contrast 2 (but no higher) could be reconstructed. This is still better than the conventional method, which fails beyond contrast 1.5, but not as good as the results at 400 MHz.

(2) Number of illuminating antennas: The input to the *CS-Net* is of size  $M \times M \times N_I$  where  $M^2$  is the number of pixels in the image and  $N_I$  is the number of illuminations. So, changing the latter number can possibly require a retraining of the network. However, under certain simplifying assumptions, such as the transmitters being placed in an equiangular manner on a circle, we can interpolate the illuminations to match the *CS-Net* requirements. Since ours is not a “black-box” approach, the physics-based parts of the algorithm should be able to reconstruct the object provided the null space components have been approximately inferred by the *CS-Net*.

(3) Number of receiving antennas: Changing this number does not alter the *CS-Net* architecture in any way, since

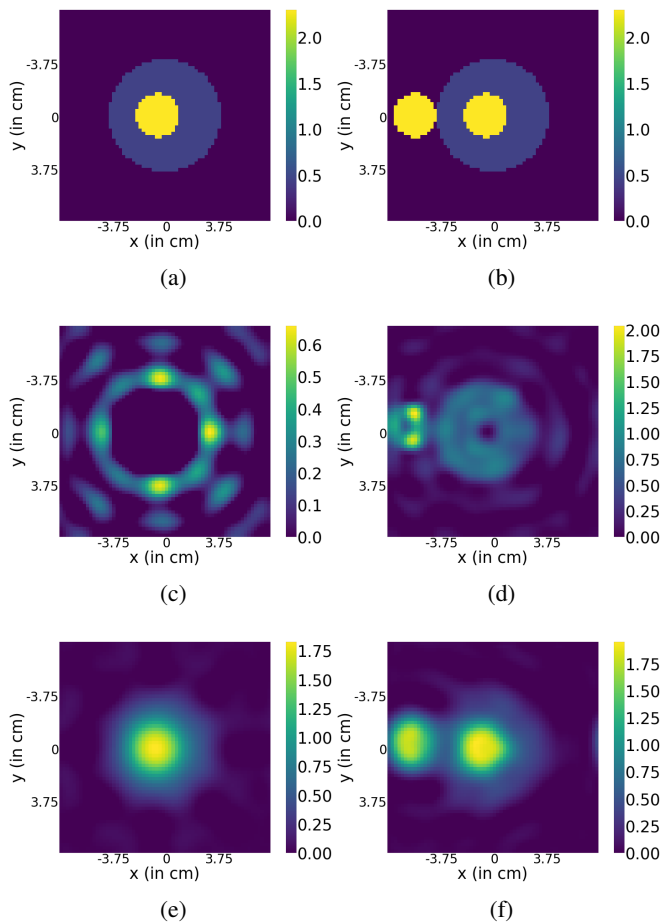


Fig. 12: (a) *FoamDieIntTM* and (b) *FoamTwinDieIntTM* profile from the Fresnel dataset. (c),(d) Respective reconstruction results at 6 GHz using proposed method without DL and (e),(f) Respective reconstruction results using proposed method with DL. The respective internal errors are (c) **0.301** (d) **0.267** (e) **0.172** (f) **0.167**.

Stage I estimates the signal space from available receiver data (provided the number of receivers is not too low and that they are uniformly spaced).

(4) Change in spatial configuration of antennas: In case there is a significant change in the location of the transmitters and receivers from what was used in the training, it becomes necessary to retrain the *CS-Net*. For instance, when using the experimental Fresnel data [45], scattered field information was available only for a field of view of  $240^\circ$  and not the entire  $360^\circ$ . In this case, we re-trained the *CS-Net* to mimic the experimental configuration.

## VI. CONCLUSION

In this paper we have introduced a deep-learning based framework that can incorporate existing iterative techniques for solving ISPs and thereby extend the range and quality of reconstructions of high permittivity objects. Specifically, we addressed the problem of strategies (like SOM) converging to false minima as the non-linearity of the ISP becomes

more pronounced when reconstructing strong scatterers. This issue was mitigated by obtaining a better estimate of the contrast source through exploiting the underlying prior with CNNs and fine-tuning the estimate by using it as initialization for iterative techniques such as SOM and TSOM with suitable regularizations. Extensive numerical experiments were conducted to demonstrate that the proposed technique could reconstruct strong loss-less (Austria profile up to contrast 4, both homogeneous and heterogeneous), lossy scatterers, as well as experimental objects.

However, a major drawback of the proposed scheme is lack of interpretability in the deep learning stage. As shown in previous Section, the proposed scheme’s reconstructions are starkly superior to its non-DL counterparts. However, the underlying prior learned by *CS-Net* in the second stage is not well-understood – leading to uncertainty as to how the CNN is able to extrapolate the entire contrast source from signal subspace. We must add however, that this is an issue that plagues much work that involves deep learning.

Future work involves formulating techniques which can reconstruct objects of much larger permittivities and sizes. One possible way is by exploiting the group sparsity prior of contrast source images using compressive sensing. Other possible direction is to increase the resolution for which *CS-Net* is trained to sizes larger than presently used, thereby allowing the CNN access to higher frequency information which wasn’t available at the current resolution of  $16 \times 16$  pixels. Additionally, there is scope to modify the existing techniques to incorporate explicit information on the objects such as box constraints on the permittivity of the scatterer and/or explicit regularization on the contrast image such as Total Variation (TV)  $\ell_1$  norm.

## ACKNOWLEDGEMENTS

The authors would like to acknowledge the Indian Space Research Organization – Space Applications Centre, for support via grant number ECO-13 titled “Soil Moisture Retrieval from Airborne Synthetic Aperture Radar.” Further, the authors are very grateful to the anonymous reviewers for their critical feedback in assessing this manuscript.

## REFERENCES

- [1] Y. Wang and W. C. Chew, “An iterative solution of the two-dimensional electromagnetic inverse scattering problem,” *International Journal of Imaging Systems and Technology*, vol. 1, no. 1, pp. 100–108, 1989.
- [2] G. Oliveri, N. Anselmi, and A. Massa, “Compressive sensing imaging of non-sparse 2d scatterers by a total-variation approach within the born approximation,” *IEEE Transactions on Antennas and Propagation*, vol. 62, no. 10, pp. 5157–5170, 2014.
- [3] D. Ireland, K. Bialkowski, and A. Abbosh, “Microwave imaging for brain stroke detection using born iterative method,” *IET Microwaves, Antennas & Propagation*, vol. 7, no. 11, pp. 909–915, 2013.
- [4] P. Shah, U. K. Khankhoje, and M. Moghaddam, “Inverse scattering using a joint  $l_1 - l_2$  norm-based regularization,” *IEEE Transactions on Antennas and Propagation*, vol. 64, no. 4, pp. 1373–1384, 2016.
- [5] W. C. Chew and Y.-M. Wang, “Reconstruction of two-dimensional permittivity distribution using the distorted born iterative method,” *IEEE transactions on medical imaging*, vol. 9, no. 2, pp. 218–225, 1990.
- [6] P. M. Van Den Berg and R. E. Kleinman, “A contrast source inversion method,” *Inverse problems*, vol. 13, no. 6, p. 1607, 1997.
- [7] P. Van den Berg and A. Abubakar, “Contrast source inversion method: State of art,” *Progress in Electromagnetics Research*, vol. 34, no. 11, pp. 189–218, 2001.

- [8] M. Li, O. Semerci, and A. Abubakar, "A contrast source inversion method in the wavelet domain," *Inverse Problems*, vol. 29, no. 2, p. 025015, 2013.
- [9] X. Chen, "Subspace-based optimization method for solving inverse-scattering problems," *IEEE Transactions on Geoscience and Remote Sensing*, vol. 48, no. 1, pp. 42–49, 2010.
- [10] Y. Zhong and X. Chen, "Twofold subspace-based optimization method for solving inverse scattering problems," *Inverse Problems*, vol. 25, no. 8, p. 085003, 2009.
- [11] Y. Zhong and X. Chen, "An fft twofold subspace-based optimization method for solving electromagnetic inverse scattering problems," *IEEE Transactions on Antennas and Propagation*, vol. 59, no. 3, pp. 914–927, 2011.
- [12] Y. Zhong, M. Lambert, D. Lesselier, and X. Chen, "A new integral equation method to solve highly nonlinear inverse scattering problems," *IEEE Transactions on Antennas and Propagation*, vol. 64, no. 5, pp. 1788–1799, 2016.
- [13] G. Oliveri, Y. Zhong, X. Chen, and A. Massa, "Multiresolution subspace-based optimization method for inverse scattering problems," *JOSA A*, vol. 28, no. 10, pp. 2057–2069, 2011.
- [14] W. Chew and J. Lin, "A frequency-hopping approach for microwave imaging of large inhomogeneous bodies," *IEEE Microwave and Guided Wave Letters*, vol. 5, no. 12, pp. 439–441, 1995.
- [15] O. M. Bucci, L. Crocco, T. Isernia, and V. Pascazio, "Inverse scattering problems with multifrequency data: reconstruction capabilities and solution strategies," *IEEE Transactions on Geoscience and Remote Sensing*, vol. 38, no. 4, pp. 1749–1756, 2000.
- [16] A. Krizhevsky, I. Sutskever, and G. E. Hinton, "Imagenet classification with deep convolutional neural networks," in *Advances in neural information processing systems*, pp. 1097–1105, 2012.
- [17] K. Simonyan and A. Zisserman, "Very deep convolutional networks for large-scale image recognition," *arXiv preprint arXiv:1409.1556*, 2014.
- [18] K. He, X. Zhang, S. Ren, and J. Sun, "Deep residual learning for image recognition," in *Proceedings of the IEEE conference on computer vision and pattern recognition*, pp. 770–778, 2016.
- [19] S. Ren, K. He, R. Girshick, and J. Sun, "Faster r-cnn: Towards real-time object detection with region proposal networks," in *Advances in neural information processing systems*, pp. 91–99, 2015.
- [20] J. Redmon, S. Divvala, R. Girshick, and A. Farhadi, "You only look once: Unified, real-time object detection," in *Proceedings of the IEEE conference on computer vision and pattern recognition*, pp. 779–788, 2016.
- [21] A. Lucas, M. Iliadis, R. Molina, and A. K. Katsaggelos, "Using deep neural networks for inverse problems in imaging: beyond analytical methods," *IEEE Signal Processing Magazine*, vol. 35, no. 1, pp. 20–36, 2018.
- [22] E. Bermani, A. Boni, S. Caorsi, and A. Massa, "An innovative real-time technique for buried object detection," *IEEE Transactions on Geoscience and Remote Sensing*, vol. 41, no. 4, pp. 927–931, 2003.
- [23] A. Randazzo and M. Pastorino, "Microwave detection of unknown targets by using support vector machines," in *Imaging Systems and Techniques, 2009. IST'09. IEEE International Workshop on*, pp. 141–146, IEEE, 2009.
- [24] S. Caorsi and P. Gamba, "Electromagnetic detection of dielectric cylinders by a neural network approach," *IEEE transactions on geoscience and remote sensing*, vol. 37, no. 2, pp. 820–827, 1999.
- [25] I. T. Rekanos, "Neural-network-based inverse-scattering technique for online microwave medical imaging," *IEEE transactions on magnetics*, vol. 38, no. 2, pp. 1061–1064, 2002.
- [26] U. Aşık, T. Günel, and I. Erer, "A wavelet-based radial-basis function neural network approach to the inverse scattering of conducting cylinders," *Microwave and Optical Technology Letters*, vol. 41, no. 6, pp. 506–511, 2004.
- [27] S. Caorsi and G. Cevini, "An electromagnetic approach based on neural networks for the gpr investigation of buried cylinders," *IEEE Geoscience and Remote Sensing Letters*, vol. 2, no. 1, pp. 3–7, 2005.
- [28] P. Shah and M. Moghaddam, "Super resolution for microwave imaging: A deep learning approach," in *Antennas and Propagation & USNC/URSI National Radio Science Meeting, 2017 IEEE International Symposium on*, pp. 849–850, IEEE, 2017.
- [29] Z. Wei and X. Chen, "Deep-learning schemes for full-wave nonlinear inverse scattering problems," *IEEE Transactions on Geoscience and Remote Sensing*, 2018.
- [30] O. Ronneberger, P. Fischer, and T. Brox, "U-net: Convolutional networks for biomedical image segmentation," in *International Conference on Medical image computing and computer-assisted intervention*, pp. 234–241, Springer, 2015.
- [31] J.-H. R. Chang, C.-L. Li, B. Poczos, B. V. Kumar, and A. C. Sankaranarayanan, "One network to solve them all-solving linear inverse problems using deep projection models," in *International Conference on Computer Vision (ICCV)*, pp. 5889–5898, 2017.
- [32] K. Zhang, W. Zuo, S. Gu, and L. Zhang, "Learning deep cnn denoiser prior for image restoration," in *IEEE Conference on Computer Vision and Pattern Recognition*, vol. 2, 2017.
- [33] J. Sun, H. Li, Z. Xu, *et al.*, "Deep admm-net for compressive sensing mri," in *Advances in Neural Information Processing Systems*, pp. 10–18, 2016.
- [34] A. Mousavi and R. G. Baraniuk, "Learning to invert: Signal recovery via deep convolutional networks," in *Acoustics, Speech and Signal Processing (ICASSP), 2017 IEEE International Conference on*, pp. 2272–2276, IEEE, 2017.
- [35] J. Richmond, "Scattering by a dielectric cylinder of arbitrary cross section shape," *IEEE Transactions on Antennas and Propagation*, vol. 13, no. 3, pp. 334–341, 1965.
- [36] K. Yaswanth and U. K. Khankhoje, "Two-dimensional non-linear microwave imaging with total variation regularization," in *Progress in Electromagnetics Research Symposium-Fall (PIERS-FALL), 2017*, pp. 1509–1513, IEEE, 2017.
- [37] T. Yin, Z. Wei, and X. Chen, "Wavelet transform subspace-based optimization method for inverse scattering," *IEEE Journal on Multiscale and Multiphysics Computational Techniques*, 2018.
- [38] S. W. Anzengruber and R. Ramlau, "Convergence rates for morozov's discrepancy principle using variational inequalities," *Inverse Problems*, vol. 27, no. 10, p. 105007, 2011.
- [39] Y. LeCun, L. Bottou, Y. Bengio, and P. Haffner, "Gradient-based learning applied to document recognition," *Proceedings of the IEEE*, vol. 86, no. 11, pp. 2278–2324, 1998.
- [40] D. P. Kingma and J. Ba, "Adam: A method for stochastic optimization," *arXiv preprint arXiv:1412.6980*, 2014.
- [41] T. M. Habashy, R. W. Groom, and B. R. Spies, "Beyond the born and rytov approximations: A nonlinear approach to electromagnetic scattering," *Journal of Geophysical Research: Solid Earth*, vol. 98, no. B2, pp. 1759–1775, 1993.
- [42] S. Boyd, N. Parikh, E. Chu, B. Peleato, J. Eckstein, *et al.*, "Distributed optimization and statistical learning via the alternating direction method of multipliers," *Foundations and Trends® in Machine Learning*, vol. 3, no. 1, pp. 1–122, 2011.
- [43] B. Wahlberg, S. Boyd, M. Annergren, and Y. Wang, "An admm algorithm for a class of total variation regularized estimation problems," *arXiv preprint arXiv:1203.1828*, 2012.
- [44] K. Belkebir and M. Saillard, "Testing inversion algorithms against experimental data," *Inverse problems*, vol. 17, no. 6, p. 1565, 2001.
- [45] K. Belkebir and M. Saillard, "Testing inversion algorithms against experimental data: inhomogeneous targets," *Inverse Problems*, vol. 21, no. 6, p. S1, 2005.

**Yash Sanghvi** is a Research Staff at the Department of Electrical Engineering at the Indian Institute of Technology Madras, India. He received his B.Tech. and M.Tech. degrees from the Indian Institute of Technology Bombay, India, in 2018. His research interests lie in the area of computational imaging, signal processing and inverse problems with application of machine learning and compressive sensing to these fields.

**Yaswanth Kalepu** (MS'18) is a graduate student at the Department of Electrical Engineering at the Indian Institute of Technology Madras, India. He received an M.Tech. degree from the Indian Institute of Technology Kharagpur, India, in 2011 and a B.Tech. degree from the Jawaharlal Nehru Technological University Kakinada, India, in 2009. His research interests lie in the area of inverse imaging and computational electromagnetics.

**Uday K Khankhoje** (M'14-SM'16) is an Assistant Professor of Electrical Engineering at the Indian Institute of Technology Madras, India. He received a B.Tech. degree from the Indian Institute of Technology Bombay, India, in 2005, an M.S. and Ph.D. degrees from the California Institute of Technology, Pasadena, USA, in 2010, all in Electrical Engineering. He was a Caltech Postdoctoral Scholar at the Jet Propulsion Laboratory (NASA/Caltech) from 2011-2012, a Postdoctoral Research Associate in the Department of Electrical Engineering at the University of Southern California, Los Angeles, USA, from 2012-2013, and an Assistant Professor of Electrical Engineering at the Indian Institute of Technology Delhi, India from 2013-16. His research interests lie in the area of computational electromagnetics and its applications to remote sensing and inverse imaging.